MICROWAVE DIAGNOSTICS OF FLARE PLASMA BY THE DIRECT FITTING METHOD BASED ON DATA FROM THE SIBERIAN RADIOHELIOGRAPH

D.A. Smirnov
N.I. Lobachevsky State University of Nizhny Novgorod,
Nizhniy Novgorod, Russia, dmitriy.smirnov@unn.ru
Central Astronomical Observatory at Pulkovo of RAS,
St. Petersburg, Russia

V.F. Melnikov
Central Astronomical Observatory at Pulkovo of RAS,
St. Petersburg, Russia, v.melnikov@gaoran.ru

Abstract. In this paper, we analyze images and the frequency spectrum of microwave emission in the maximum of brightness distribution in the January 20, 2022 and July 16, 2023 flares recorded by the Siberian Radioheliograph in the 3–6 GHz and 6–12 GHz ranges. We use the obtained spectrum data for radio diagnostics of magnetic field strength and orientation, plasma density, and parameters of accelerated particles in a radio source. The radio diagnostics is carried out by a method based on minimizing the functional containing the intensities of theoretically calculated and observed frequency spectra of left-polarized and right-polarized emission. Since the form of such a multidimensional functional is quite complex, and it is not possible to minimize it by standard approaches, we employ a genetic minimization method. The radio diagnostics allows us to determine features of the dynamics of the magnetic field intensity and orientation, as well as the density and the energy spectral index of non-thermal electrons in the region of maximum brightness of the radio source. We have found that during the growth phase of the main radiation peaks the magnetic field decreases, whereas during the decay phase, on the contrary, it increases. The rate of these changes varies from a few G/s to 11 G/s for the January 20, 2022 flare and is about 1 G/s for the July 16, 2023 flare.

Keywords: solar flares, radioheliograph, radio diagnostics, magnetic field.

INTRODUCTION

The development of methods for radio diagnostics of solar flares has become extremely relevant recently. Especially important is the possibility of using these methods to obtain detailed information on the coronal magnetic field and electrons of moderately relativistic energies, which is impossible in other electromagnetic spectral regions. The problem of measuring the magnetic field dynamics in coronal radio sources, in particular the rate of change in its intensity, is directly related to the rate of dissipation of free magnetic energy during a flare and hence to the mechanism of energy release and acceleration of particles in flares.

To solve this problem, a method of determining flare loop plasma parameters, which is based on the developed theory of gyrosynchrotron (GS) emission [Fleishman, Melnikov, 2003] and on created fast computer codes [Fleishman, Kuznetsov, 2010], is employed. This method of radio diagnostics allows us to fit calculated and observed emission spectra and thereby to obtain data on the intensity and orientation of the magnetic field, plasma density, and parameters of energetic electron fluxes in a radio source. The method has been proposed and examined using model sources in [Fleishman et al., 2009; Gary et al., 2013]. Morgachev et al. [2014] applied the method to the analysis of the July 19,2012 flare, recorded by the Nobeyama Radioheliograph (NoRH). As a result of the analysis, plasma and magnetic field parameters in the flare loop were restored, and the fact of longitudinal pitch-angle distribution of radiating high-energy electrons was established. The application of the method to the September 10, 2007 solar flare, recorded by the imaging spectrometer Extended Owens Valley Solar Array (EOVSA) [Fleishman et al., 2020, 2022], has revealed an unexpectedly high rate of decrease in the magnetic field in the region of the brightest microwave radiation source. This allowed the authors to conclude about the high rate of magnetic energy dissipation, which can lead to the appearance of a super-Dreicer electric field and to very efficient plasma heating and particle acceleration. It is interesting to note that the directly opposite dynamics of the field strength, namely, its increase in the upper part of the loop, is predicted by the well-known model of electron acceleration [Somov, Kosugi, 1997; Bogachev, Somov, 2005] by the betatron mechanism due to the collapse of the field lines reconnected in the current sheet.

Unfortunately, radio diagnostics of this type has been carried out for too few flares (we are aware of only two reported events). New observations and appropriate diagnostics of other flares are required. Recently, new opportunities have been opened up for this. They are primarily associated with the creation of multifrequency radioheliographs, which replace NoRH that conducted spatially resolved observations of flares at 17 and 34 GHz frequencies until 2019. To date, observations have been initiated at the Siberian Multifrequency Radioheliograph (SRH, 3–6, 6–12, 12–24 GHz) [Altyntsev et al., 2020] and the Chinese Spectroheliograph (MUSER, 0.4–2, 2–15 GHz) [Yan et al., 2021]. Regular observations are being made with the 13-element American Solar Imaging Spectrometer EOVSA (1–18 GHz) [Gary et al., 2018].

This work is aimed at microwave diagnostics of flare plasma by the direct fitting method from SRH data on the January 20, 2022 and July 16, 2023 flares. Section 1 describes an algorithm for restoring parameters of plasma and accelerated particles. In section 2, the method is applied to the diagnostics of parameters of a model radio source. Sections 3–5 analyze SRH observational data and restore parameters in radio sources of the January 20, 2022 and July 16, 2023 flares. In conclusion, we summarize the results and discuss possible causes of the detected significant magnetic field variations in the maximum brightness region of the radio sources.

1. PARAMETER RESTORATION METHOD

The developed algorithm of radio diagnostics involves fitting the GS emission intensities, calculated using Fast GS Codes [Fleishman, Kuznetsov, 2010], and the observed values at a set of frequencies with available observational data.

Mathematically, the problem can be described as minimization of the functional written as follows:

$$K = \sum_{i=1}^{n} \left| \left(I_L^i \left(x_1, x_2, ..., x_n \right) + I_R^i \left(x_1, x_2, ..., x_n \right) j \right) - \left(I_{L_{obs}}^i + I_{R_{obs}}^i j \right) \right|, \quad (1)$$

where I_L and I_R are intensities of left-handed and right-handed polarized theoretically calculated emission; $I_{L_{obs}}$ and $I_{R_{obs}}$ are intensities of left-handed and right-handed polarized emission observed in the source; x_1, x_2, ..., x_n are medium parameters inside the radio source.

Since such a functional, especially with a large number of parameters x_1, x_2, ..., x_n, is very complex and it is impossible to use standard methods to minimize it, we have applied the genetic minimization algorithm proposed in [Morgachev et al., 2014], but the algorithm was somewhat modified. Let us describe this algorithm step by step.

First, a given number of points (sets of plasma parameters inside a source) are generated in a region of multidimensional parameter space. The region is selected based on estimates of the parameters obtained by the initial manual fitting. The generation is carried out randomly according to normal or lognormal distributions. The lognormal distribution is necessary for uniform filling for the parameters with a large range of possible values (several orders of magnitude).

Then, for each set of parameters, emission intensities at different frequencies, as well as functionals are calculated. A certain number of points with the lowest functional are selected, and further generation occurs around them randomly according to normal distribution with a width depending on the distance to the nearest points with the lowest functional in the parameter space. Mathematically, the probability density of this distribution can be described as follows:

$$p(x) = \frac{1}{\sqrt{2\pi (rC)^2}} \exp\left(-\frac{(x-\mu)^2}{2(rC)^2} \right),$$

where μ denotes coordinates of the selected point; r is the average distance to the nearest selected points; C is the specified coefficient; rC designates the standard deviation σ. This selection and generation process is repeated until the functional stops decreasing. Note that this may be due to finding both the true solution and the lowest value of the calculated function, as well as the most correct solution within existing measurement errors in the observed radio frequency spectrum.

1. EXAMINATION OF THE MODEL SOURCE

SRH observations do not always cover the entire frequency range around the spectral peak frequency f_{peak} from $f<f_{peak}$ to $f>f_{peak}$. It happens that it is limited to a relatively narrow region. That is why, to verify the possibility of restoring the parameters of the magnetic field, plasma and energetic electrons inside a radio source from data on the frequency spectrum in a limited frequency range, we have analyzed two model radio sources with different specified parameters (Table 1) for the following typical cases (Figure 1). In the first case, the restoration was based on data only in the spectral range to f_{peak} (section 1). Self-absorption or the Razin effect usually dominates in this range [Razin, 1960; Kuznetsov, Melnikov 2012]. In the second case, the range also includes a region in the vicinity of f_{peak}, where the source is already partially optically thin (sections 1, 2). In the third case, the range is examined that includes a region near f_{peak} and a spectral region, where the source is optically thin (sections 2, 3). In the fourth, there is only the range $f>f_{peak}$ (section 3). In the fifth, there are all ranges (sections 1, 2, 3).

When restoring from model sources, the radioheliograph was assumed to have a sufficiently high angular resolution and the radio source is resolved at all frequencies. Moreover, we supposed that within the beam pattern it is uniform in all its parameters (magnetic field strength and orientation, plasma density, energy spectrum of non-thermal electrons, etc.). This is a simplified approach, but it allows us to identify some features.

The following conditions have been selected. Isotropic pitch-angle distribution of energetic electrons. The electron energy spectrum was defined as double power law with the break at energy E_{break}, i.e. it consisted of two parts ($E<E_{break}$, $E>E_{break}$), where both the high-energy and low-energy parts were described by power laws with different spectral indices δ_1 and δ_2. Minimum and maximum limits in the electron energy distributions E_{min} and E_{max} are 30 keV and 10 MeV respectively. The boundary of the loss cone is 10°.

The analyzed homogeneous regions of the model sources had the same depth $D=3\cdot10^8$ cm, area $S=2.76\cdot10^{17}$ cm^2, number density of non-thermal electrons $n_b(E>0.1\text{MeV})=8\cdot10^6$ cm^{-3}, and temperature of the background plasma. Nonetheless, other parameters (electron density of background plasma n_0, magnetic field strength B, angle θ between magnetic field direction and line of sight θ, double power law break energy E_{break}, and spectral indices δ_1 and δ_2) differ in the models (see Table 1).
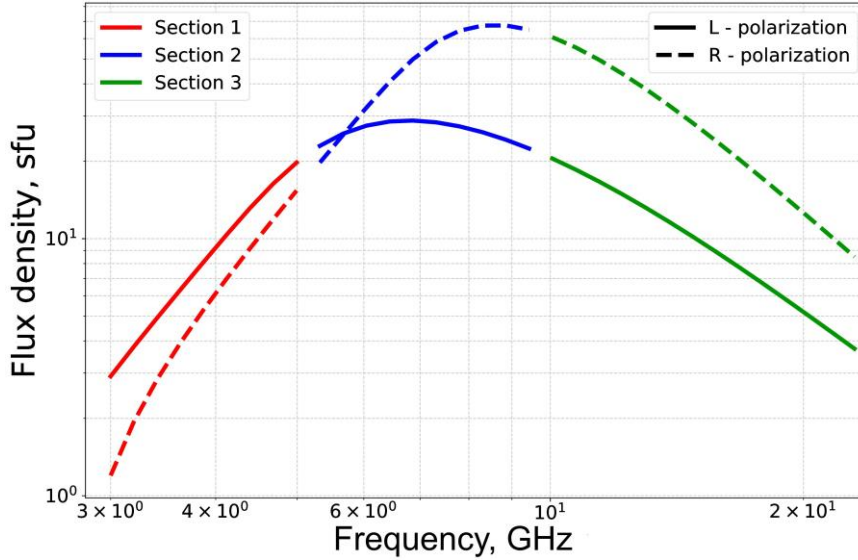
Figure 1. Partitioning of the frequency spectrum into sections to examine model sources

The difference between model 2 and model 1 one consists, first of all, in a significant increase in the ratio of the plasma electron density to the magnetic field strength (8.75 times). This is done in order to enhance the Razin effect and evaluate its role in conducting diagnostics. According to calculations of GS emission using fast GS codes [Fleishman and Kuznetsov, 2010], in model 1 the spectral peak frequency turned out to be 10.2 GHz for left-handed polarized emission and 12.1 GHz for right-handed polarized emission, and for model 2 these values were 6.8 and 8.6 GHz respectively.

For each of the two models, we have calculated emission intensities in the right- and left-hand polarizations at frequencies that coincide with the SRH frequencies. These intensities were assumed to be observable. Then, according to the procedure described in Section 1, these observed values were used to restore the above seven parameters of the medium and energetic electrons inside the model radio sources, assuming that their values are unknown. Tables below list relative deviations of the restored values from those given for each of the two models of radio sources. The deviations were calculated using the formula

$$\delta = \frac{A_{\mathrm{d}} - A}{A} \cdot 100\,\%, \tag{2}$$

where A_{d} is a restored parameter; A is a model parameter.

Table 1

Parameters of model radio sources

Model No.	T_0, K	n_0, cm^{-3}	B, G	θ, deg.	n_{b}, cm^{-3}	E_{break}, MeV	δ_1	δ_2
Model 1	1e7	1e10	350	85	8e6	0.3	4	8
Model 2		5e10	200	65	8e6	0.5	3	5

Table 2

Relative deviations of the restored values from those for model 1

Spectral regions	n_0	B	θ	n_{b}	E_{break}	δ_1	δ_2
1 (3–8.3 GHz)	41.5 %	0.2 %	3.2 %	0.2 %	64.9 %	0.01 %	47.4 %
1, 2 (3–13.8 GHz)	2.6 %	0.07 %	0.1 %	0.04 %	4.3 %	0.1 %	17.2 %
2, 3 (8.8–23 GHz)	267 %	55.2 %	32.3 %	64 %	233 %	13 %	325 %
3 (14.7–23 GHz)	937 %	17.8 %	5.3 %	238 %	35.8 %	15.4 %	75.6 %
1, 2, 3 (3–23 GHz)	0.7 %	0.1 %	0.09 %	0.4 %	2.0 %	0.03 %	3.9 %

Table 3

Relative deviations of restored values from those for model 2

Spectral regions	n_0	B	θ	n_{b}	E_{break}	δ_1	δ_2
1 (3–5.7 GHz)	32.5 %	5.5 %	10.0 %	3.5 %	144 %	1.8 %	432 %
1, 2 (3–8.3 GHz)	0.7 %	0.8 %	1.2 %	5.7 %	65.5 %	1.1 %	904 %
2, 3 (5.7–23 GHz)	31.6 %	47.9 %	22.8 %	1100 %	22.5 %	43.9 %	431 %
3 (13.8–23 GHz)	34.8 %	34.3 %	14.0 %	2000 %	233 %	41.9 %	194 %
1, 2, 3 (3–23 GHz)	6.2 %	3.8 %	1.3 %	13.3 %	4.8 %	3.1 %	1.3 %

From Tables 2 and 3 it can be seen that for the case when all spectral regions 1–3 are involved, the error proved to be very low, not exceeding several percent for all seven parameters being restored. This result is quite expected since when minimizing functional (1), expressions for intensity at $f<f_{peak}$ and $f>f_{peak}$ were simultaneously used in the system of equations at which this emission characteristic depends on the radio source parameters in markedly different ways. The equations in these two ranges prove to be independent. This is what provides a minor error in parameter restoration. To illustrate the fact of independence, let us take a look at simplified expressions [Dulk, 1985] for emission intensity at frequencies, where the source is optically thick and optically thin respectively. At $f>f_{peak}$, the emission flux density F_f is proportional to the expression

$$
F_f \propto N(E>E_0)B(\sin\theta)^{-0.43+0.65\delta} \times \\
\times (f/f_b)^{1.22-0.90\delta} LS_s,
\tag{3}
$$

where $f_b=eB/(2\pi mc)$ is the gyrofrequency; e and m are electron charge and mass; L and S_s are source depth and area. There is an obvious strong direct dependence of F_f on the magnetic field ($F_f \propto B^{0.90\delta-0.22}$) and on the angle of view for any reasonable values of δ.

At $f<f_{peak}$, the dependence on B and θ is distinctly different:

$$
F_f \propto (\sin\theta)^{-0.36-0.06\delta} \cdot f^2 \left(\frac{f}{f_b}\right)^{0.50+0.085\delta} \cdot S_s,
\tag{4}
$$

it becomes inverse. For the magnetic field dependence, we obtain $F_f \propto B^{-0.5-0.085\delta}$. Note that with a high ratio of plasma density to magnetic field strength, in the frequency range $f<f_R=20\,n_0/B$, when the Razin effect is significant, the F_f dependence on the parameters in the source becomes even more complex and very different from (3).

As follows from Tables 2, 3, the error in restoring the source parameters for some model parameters — magnetic field B, angle of view θ, electron spectrum index δ_1 — increases when not all spectral regions are involved in the restoration, but it still proves to be quite acceptable for all the cases and models considered. In particular, when restoring parameters in a growing part of the spectrum (range 1), the error does not exceed 3.2 % for the first model and 10 % for the second model. In our opinion, this is a good result demonstrating the potential for diagnostics even without optically thin part of the spectrum, which often happens in practice when the spectral peak frequency f_{peak} is not within the range of observations. The error is expected to decrease for range 1–2 since at the upper boundary of the range the source becomes partially optically thin, and when restoring the parameters it is possible to use independent equations.

On the other hand, for ranges 2–3 and 3 the error in restoring the parameters B, θ, and δ_1 increases significantly (to ~30–50 %). The reason lies presumably in the high degree of dependence of the equations on each other at different frequencies, at which the source is optically thin. This is especially evident when the parameters $n_b(E>0.1$ MeV), E_{break}, and δ_2 are restored.

Particularly noteworthy is the high error in determining the plasma density in model 1 as compared with model 2. The reason is that in model 1 the emission intensity almost does not depend on the plasma density in most of the spectrum due to the weak Razin effect as compared to model 2.

2. EVENT SELECTION AND THEIR PRELIMINARY ANALYSIS

Two flare events observed by SRH have been selected for radio diagnostics. The selection was carried out according to the following criteria: a) the presence of one or more clear peaks in the time profile of density of the integral emission flux from a flare, as well as pronounced rise and decay phases; b) duration of the burst sufficient to analyze the dynamics of the restored parameters; c) satisfactory quality of radio maps synthesized from SRH data.

The January 20, 2022 flare event, which occurred in the northwestern part of the solar limb, was of the GOES class M5.5. Its source was NOAA Active Region (AR) No. 12929 (Figure 2). SRH observed the flare in the frequency range 6–12 GHz. The time profiles of radio emission at 6–12 GHz, obtained from correlation amplitude data, are presented in Figure 3. It can be seen that the radio burst consists of at least three superimposed emission peaks. The total duration of the burst is ~15 min. Eight instants of time have been selected for radio diagnostics: 4 for burst maxima, 2 for rise phases, and 2 for decay phases. These instants are indicated by vertical lines: solid lines are the instants of maxima of individual peaks in time profiles; dashed lines are the instants during rise phases; dotted lines are the instants during decay phases of the peaks. Dynamics of the AR is illustrated in Figure 4 for 6.2 GHz and in Figure 5 for 10.6 GHz. The size of the boxes for each selected instant of time is 98"×98".
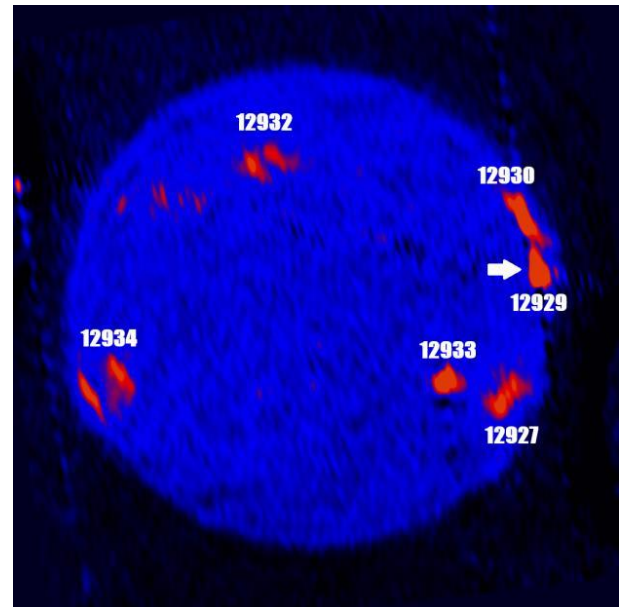

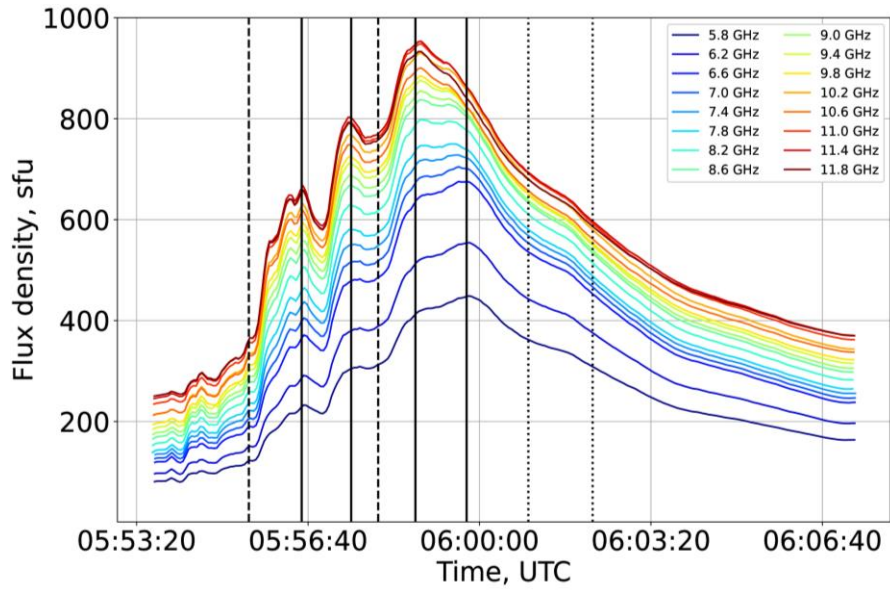*Figure 2.* Radio map of the Sun at 6.2 GHz for January 20, 2022

Figure 3. Time profiles of the integral emission flux density for the January 20, 2022 flare
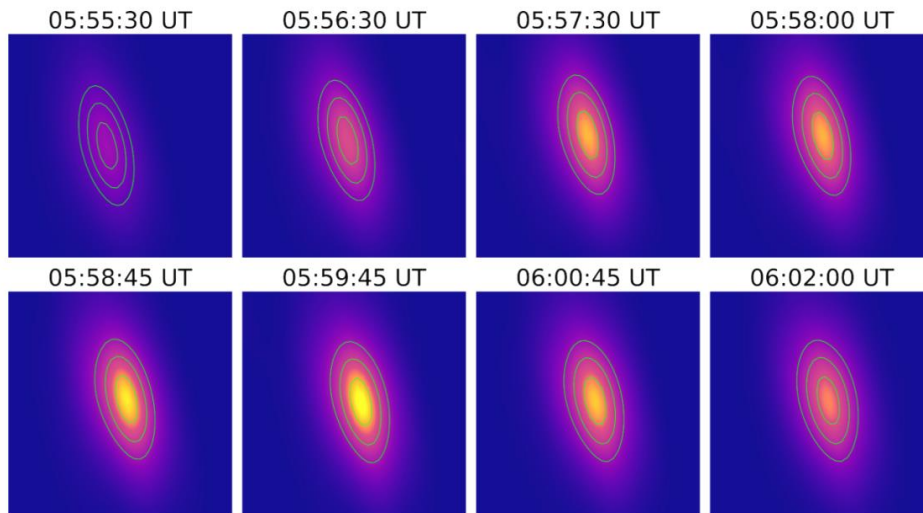

Figure 4. Radio images of the January 20, 2022 flare at different instants of time at a frequency of 6.2 GHz. Contours denote the 0.5, 0.7, 0.9 levels of maximum brightness
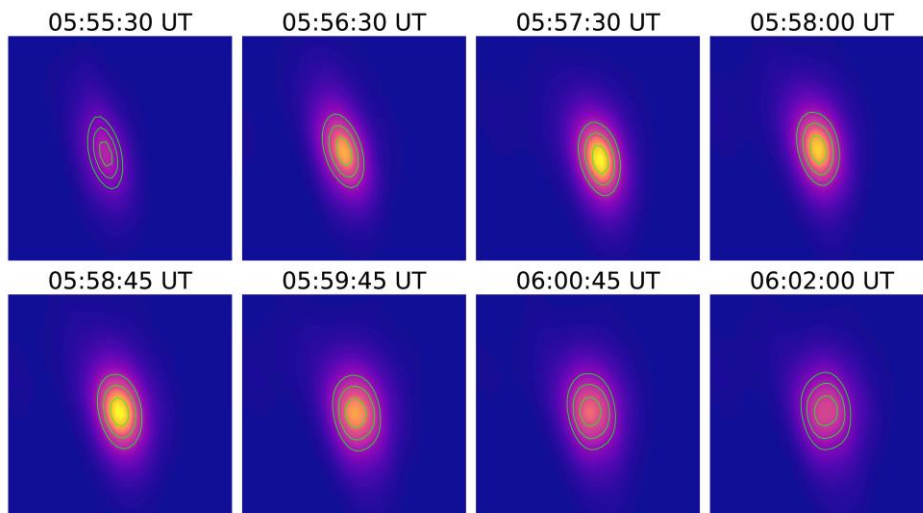

Figure 5. The same at 10.6 GHz

The July 16, 2023 flare event, which occurred in the northeastern part of the solar disk, was of GOES class M1.1. Its source was AR NOAA No. 13372 (Figure 6). SRH observed the flare in the frequency range 3–12 GHz, i.e. two antenna arrays were employed: 3–6 and 6–12 GHz. The time profiles of radio emission at frequencies 6–12 GHz are shown in Figure 7. The radio burst is short, ~2.5 min, i.e. six times shorter than in the January 20,

2022 flare. However, it also consists of several emission peaks, each lasting for 30–50 s. For the radio diagnostics, we have selected 10 instants of time: 3 for the burst maximum, 4 for rise phases, and 3 for decay phases. Dynamics of the AR is illustrated in Figure 8 for 6.2 GHz and in Figure 9 for 10.6 GHz. The size of the boxes for each selected instant of time is 49"×49".
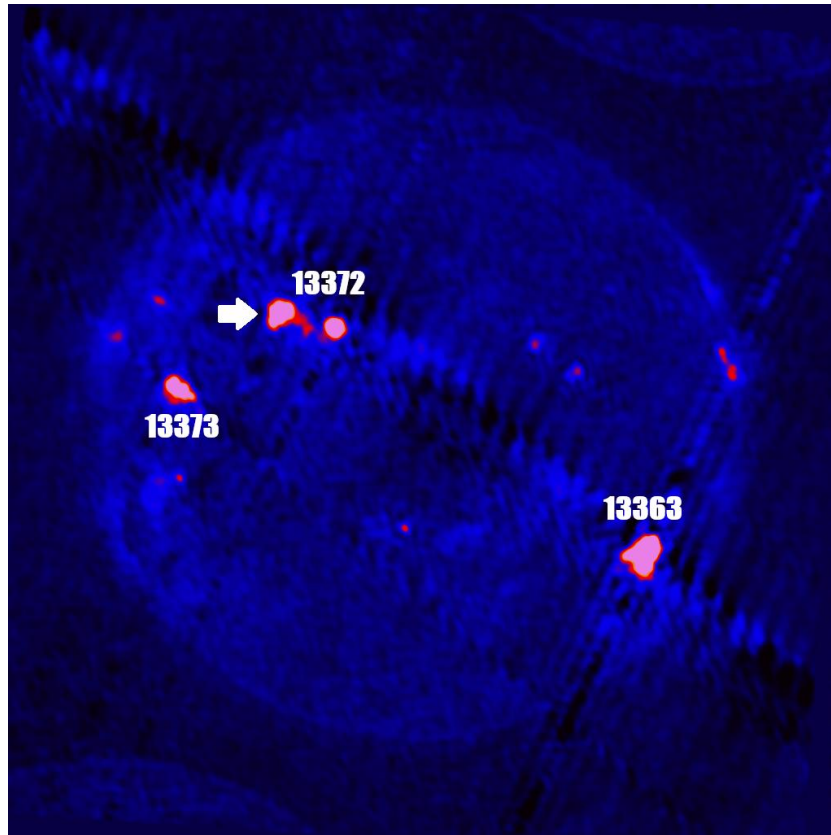
Figure 6. Radio map of the Sun on July 16, 2023 at 6.2 GHz
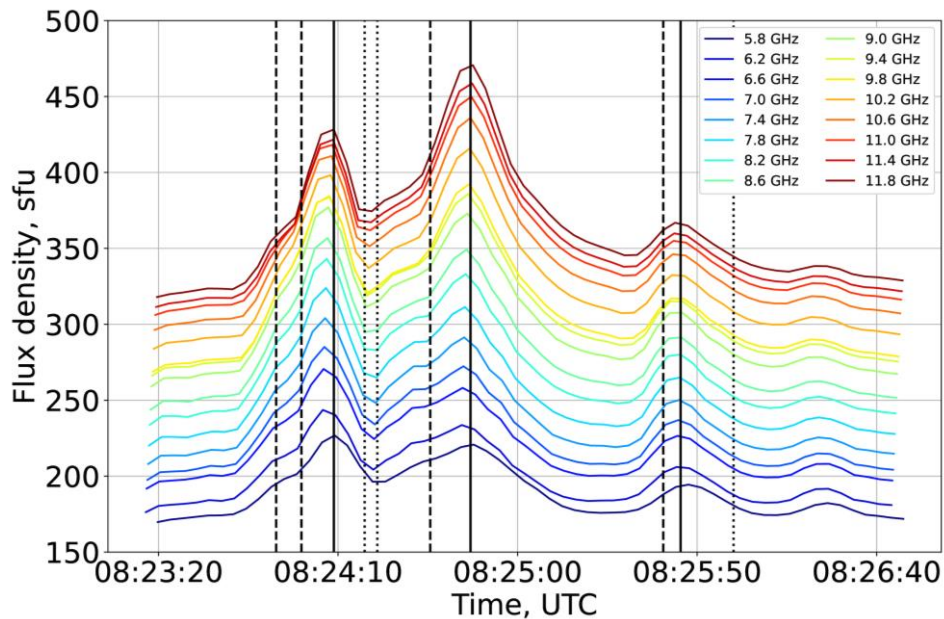
Figure 7. Time profiles of the integral radio emission flux density for the July 16, 2023 flare
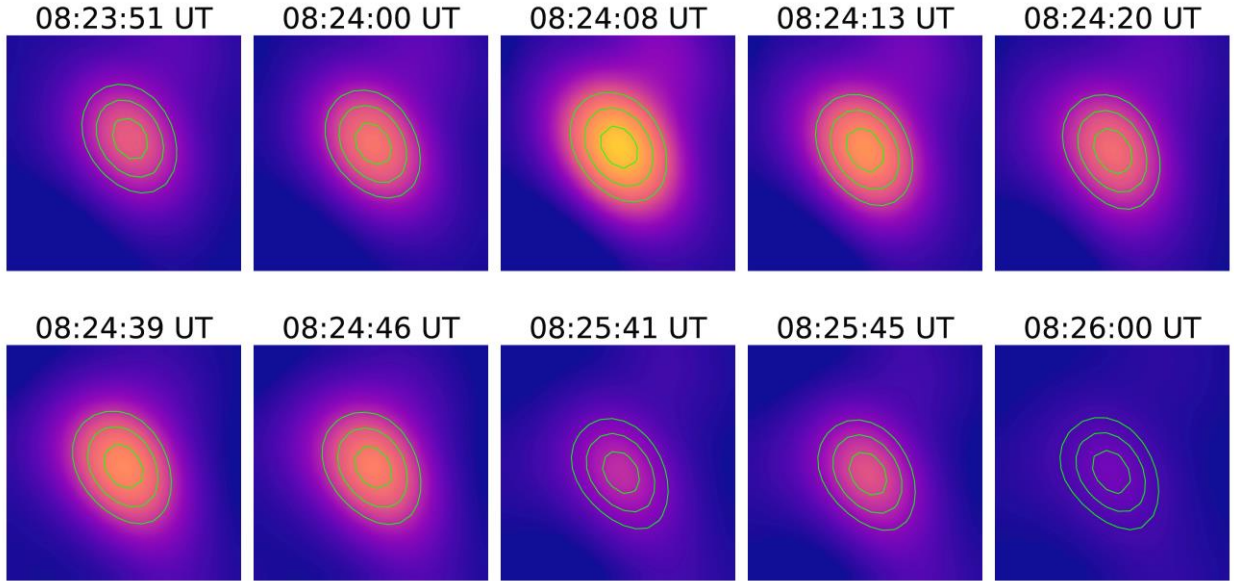
Figure 8. Radio images of the July 16, 2023 flare for different instants of time at 6.2 GHz. Contours denote the 0.5, 0.7, 0.9 levels of maximum brightness
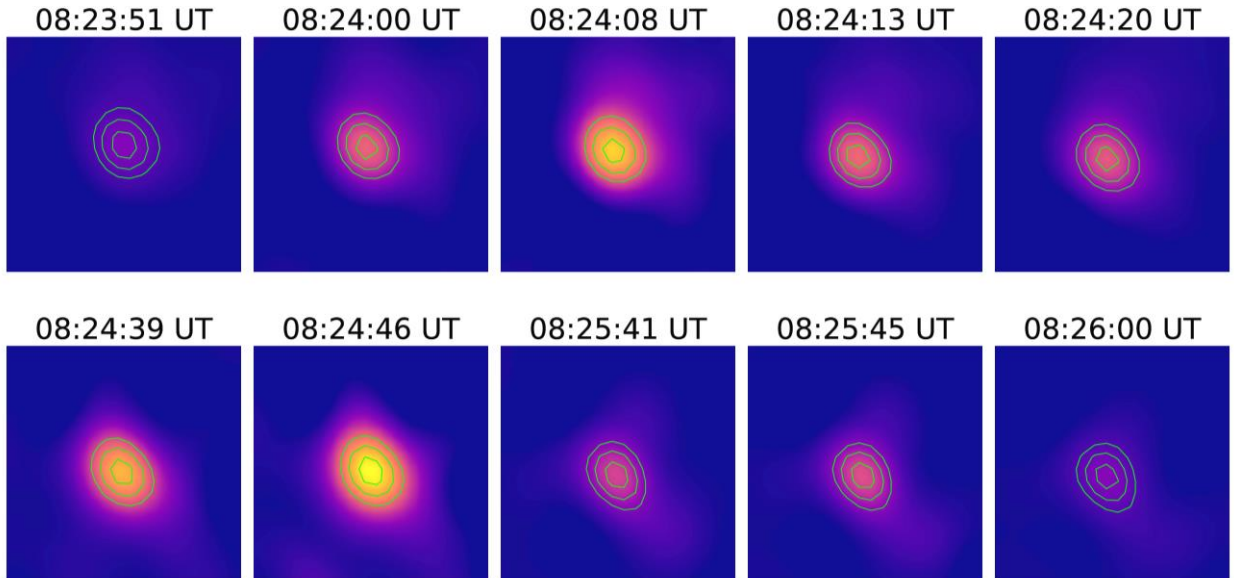

Figure 9. The same at 10.6 GHz

For both events, contours in Figures 4–5, 8–9 depict the brightness temperature levels 0.5, 0.7, 0.9 of the maximum. It is noteworthy that 1) brightness temperature distribution during both flares has a well-defined maximum throughout the flare; 2) maximum brightness temperature for these points is $4.6 \cdot 10^7$ K for the January 20, 2022 flare and $5.4 \cdot 10^7$ K for 6.2 and 10.6 GHz respectively. For the July 13, 2023 flare, $4.3 \cdot 10^7$ and $5.5 \cdot 10^7$ K for 6.2 and 10.6 GHz respectively; 3) the characteristic source size at 6.2 GHz is almost twice as large as at 10.6 GHz. Of course, the difference between beam widths of the two SRH antenna arrays should play a certain role in this. Nonetheless, given that for the July 16, 2023 flare the half-amplitude beam pattern is 23.1"×16.5" and 13.4"×9.8" at 6.2 and 10.6 GHz respectively, the source can be considered to be partially resolved since it is commensurate or slightly smaller than the corresponding source dimensions (27.0"×24.5" and

14.7"×12.3"). The same can be said about the January 20, 2022 flare, where the half-amplitude beam pattern is 52.0"×16.2" and 13.4"×9.8" at 6.2 and 10.6 GHz respectively, and the source dimensions are 51.5"×27.0" and 34.3"×19.6" respectively.

3. CONSTRUCTION AND CALIBRATION OF RADIO IMAGES

Before the procedure for obtaining the frequency spectrum in order to further restore it by the method we have developed, it is necessary to implement a package of measures for preparing radio images. Firstly, we synthesized radio images at each frequency, using the method and software package developed at ISTP SB RAS [Altyntsev et al., 2020]. In particular, at the stage of image synthesis at each frequency, images in R and L polarizations were aligned relative to each other by min-

imizing linear slopes in the phase difference of antennas in different polarizations. Since these phases differ little, it is possible to see a linear slope explicitly as it leads to a shift of the entire image in the phase spectrum according to the shift theorem [Christiansen, Högbom, 1988]. In practice, this method often gives an error; therefore, it is combined with manual alignment by fitting the solar disk image in the left-hand polarization to the image in the right-hand polarization, using a difference image built between them, in which the shift is clearly seen.

Secondly, we calibrated brightness temperature values of the entire solar image. Since most of the image is occupied by quiet regions, the most common brightness temperature corresponds to the brightness temperature in quiet Sun regions. All values in the data array were rounded to two decimal places, and then the mode value was found, which was taken as the brightness temperature of the quiet Sun at a given frequency. Next, the obtained value was correlated with the theoretical one according to the interpolated function of the brightness temperature dependence on frequency derived on the basis of [Zirin et al., 1991]. From the deviation of the theoretical value from the observed one, we calculated a calibration coefficient and multiplied the distribution of the initial measured brightness temperature of the entire image of the Sun by it.

The images were then aligned at different frequencies because it turned out that the position of brightness centers can vary greatly from frequency to frequency. This is unacceptable for radio diagnostics since parameters of flare plasma and energetic electrons should be restored for the same place in AR. The image alignment method mentioned above is not suitable for images at different frequencies as antenna phases may differ markedly at different frequencies. The alignment was therefore carried out with respect to a stable local radio source remote from the flare; for the source we chose a compact gyroresonance microwave source over a solitary sunspot. The characteristic time of its change is quite long, from hours to several days, which is much longer than the processes occurring in the flare. Images of this source at different frequencies were superposed in the coordinates of the brightest pixel and thus deviations were determined. These deviations were then considered as corrections in the coordinate grid of the flare radio image at each frequency.

To restore the parameters of flare plasma in the radio source, we used the frequency spectrum of the flux density from the selected area of the flare radio image of size from one to several pixels. The frequency spectrum was calculated by converting the brightness temperature in this area into solar flux units (1 s.f.u. = 10^{-22} W m^{-2} Hz^{-1}) by the formula

$$F(f) = \left(\frac{2kT_\mathrm{b} f^2}{c^2} \right) \Omega, \qquad (5)$$

where $k=1.38 \cdot 10^{-16}$ erg/K is the Boltzmann constant; T_b is the brightness temperature in kelvins; f is the frequency of observations; c is the velocity of light in free space, Ω is the angular size of the source area in steradians: $\Omega = \Delta x \, \Delta y / R^2$, where Δx, Δy are pixel dimensions [cm], R is the Earth — Sun distance.

4. RESTORATION OF PARAMETERS FOR THE FIRST AND SECOND FLARES

Using the method described in Sections 1 and 2, we have restored parameters for the selected flare events. For this purpose, we employed frequency spectra of the emission flux density from the flare radio image area corresponding to 3×3 pixel (1 px=2.5", S=2.76·10^{17} cm^2) near the brightest point in AR at 8.6 GHz. The frequency spectrum thus obtained was approximated by a polynomial function to eliminate the spread of observed values related to instrumental measurement errors. Note that the brightness temperature T_b we use is derived from convolution of the true brightness temperature distribution with the beam pattern of the radioheliograph. It is, therefore, a value averaged over the cross-sectional area of the beam pattern. T_b at each frequency was believed to be close to the true brightness temperature at the brightness center of the source since the beam width of the radio interferometer during observations was commensurate or slightly smaller than the size of the observed source (see Section 3). For theoretical calculations of the GS emission spectrum of a source with an area S=2.76·10^{17} cm^2, we adopted a simple model of a rectangular parallelepiped homogeneous in depth with a side h=3·10^8 cm. In a real source, the desired parameters are certainly more or less nonuniform. Therefore, as a result of the restoration, we get some averaged values of the parameters.

For the January 20, 2022 flare, the region including the spectral peak f_peak entered the observation frequency range 6–12 GHz only at 05:55:30 UTC. At all other times, the range of observations was exclusively within $f < f_\mathrm{peak}$. For the July 16, 2023 flare, the observation range 3–12 GHz includes f_peak for the first four time points, i.e. 08:23:51–08:24:13 UTC.

During the radio diagnostics, a different number of generations (from 10 to 40) were required for each flare and for each time point, depending on the convergence rate of the algorithm. Referring to Figure 10, the decreasing rate of the functional gradually goes down and the minimization process stops when the functional ceases decreasing at a certain level, which, in particular, is due to the existing measurement errors in the observed frequency spectrum of radio emission.

An example of fitting theoretical spectra to those observed at selected time points is given in Figure 11 for the January 20, 2022 flare and in Figure 12 for the July 16, 2023 flare. The plots are for the total (R+L) flux density, and yet fitting in accordance with Formula (1) was performed for L and R polarizations separately. The resulting spectrum is indicated by the black line.

Figures 3 and 13 show that at the beginning of the January 20, 2022 flare during the rise phase of the radio emission flux density the magnetic field weakened from ~990 to ~360 G. This corresponds to the decreasing rate of the field $\Delta B / \Delta t \approx -11$ G/s. Then, after passing the first peak at 05:56:30 UTC, the field begins to increase. At the minimum between the second and third peaks (05:58:00 UTC), the field reaches a local maximum of
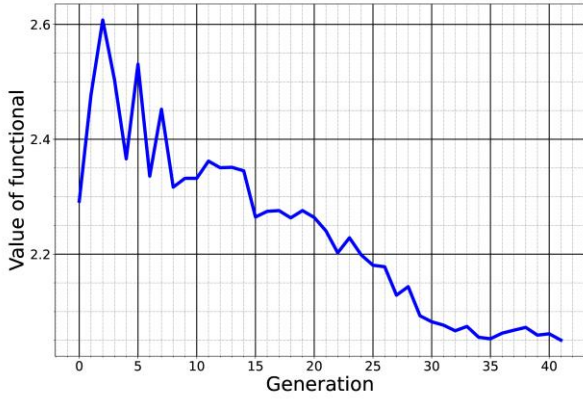
Figure 10. Behavior of the functional during radio diagnostics for 05:56:30 of the January 20, 2022 flare
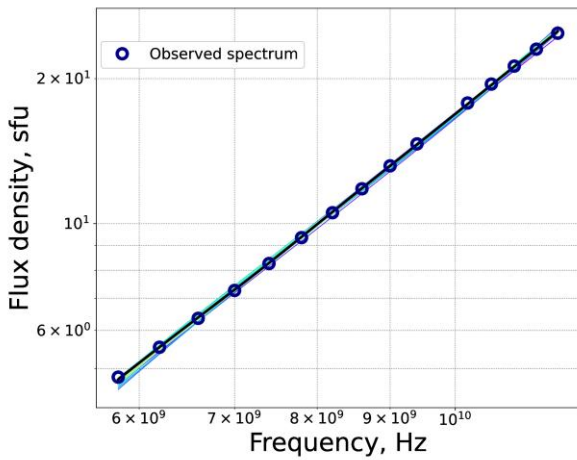

Figure 11. Illustration of the fitting of theoretically calculated spectra to the observed one for 05:58:00 of the January 20, 2022 flare
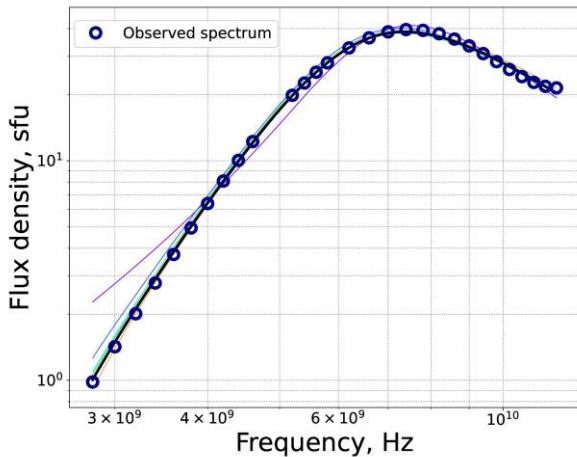

Figure 12. The same for 08:23:51 of the July 16, 2023 flare

580 G and begins to weaken at a rate $\Delta B/\Delta t \approx -7$ G/s. At the peak of the burst (third peak, 05:58:45 UTC), the field is the lowest (B=280 G), and after passing through the peak it begins to rise again at a rate $\Delta B/\Delta t \approx 3.6$ G/s for 3 min, reaching ~1020 G in the end. Thus, there is

the following pattern. At each peak of the burst, the field decreases, and during the decay phase of peak intensity it increases, with the rate of these changes varying from a few to ten G/s.

In general, for this event the energy spectrum of electrons is unusually steep, the spectral index δ_1 decreases during the rise phase, starting from 22 and reaching 8.5 at the burst peak; and during the decay phase of the main emission peak (05:59:45–06:02:00 UTC), it increases to 10.8. Note also that during this time interval there is a monotonous increase in the angle θ (from 113° to 174°), which means that the angle between the line of sight and the direction of field lines decreases from 67° to 6°.

For the July 16, 2023 flare, the parameters B, θ, and δ_1 (Table 4) are quite different from the corresponding parameters for January 20, 2022 flare (Table 5). The magnetic field is smaller by an order of magnitude, and the energy spectrum index is 2–4 times lower. No strong changes in θ and δ_1 were recorded. Nonetheless, the relative variations in B are also significant.

In general, the dynamics of the magnetic field is similar to the dynamics of the field in the radio source of the January 20, 2022 flare. This is evident at least for two most intense emission peaks. For the first peak (t_{max}=08:24:08 UTC), the field decreases slightly from 84 to 78 G during the rise phase and increases during the decay phase. This decrease in the field during the rise phase is most pronounced for the second peak (t_{max}=08:24:39-08:24:46 UTC): the field first decreases from 84 to 51 G, and then increases to 83 G. Unfortunately, between 08:24:46 and 08:25:41 UTC we failed to restore the field values. We cannot, therefore, say anything about its dynamics during the decay phase of the second peak. However, further on, during the decay phase of the third peak (t_{max}=08:25:41 UTC), the field rises rapidly and reaches 147 G. In general, after the main peak of the flare the field increased threefold, and the average rate of its variation was $\Delta B/\Delta t \approx 1.2$ G/s. The maximum rate of field decrease observed at 08:24:08–08:24:39 UTC $\Delta B/\Delta t \approx -1.2$ G/s.

Unfortunately, our approach cannot yet assess errors for the parameters being restored. The accuracy of the restoration is estimated by the method of relative shift: by changing one parameter and leaving the others unchanged, we can determine the contribution of a particular
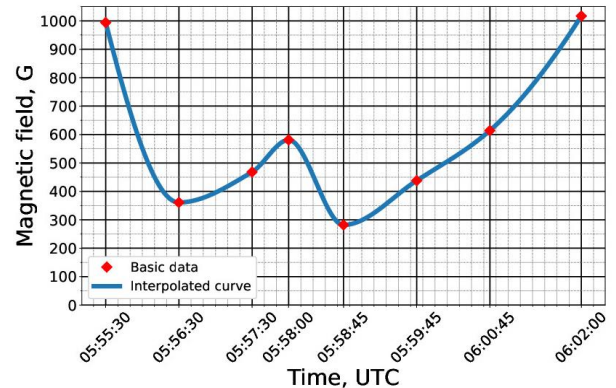

Figure 13. Magnetic field variation during the January 20, 2022 flare

Table 4

Restored parameters for the July 16, 2023 flare

UTC	B, G	θ, deg.	δ_1
08:23:51	84	135	4.97
08:24:00	79	143	4.78
08:24:08	78	132	4.97
08:24:13	84	137	3.95
08:24:20	78	139	4.26
08:24:39	51	137	3.99
08:24:46	70	136	4.28
08:25:41	83	126	4.60
08:25:45	104	130	4.30
08:26:00	147	130	3.98

Table 5

Restored parameters for the January 20, 2022 flare

UTC	B, G	θ, deg.	δ_1
05:55:30	994	92	22.1
05:56:30	361	105	10.2
05:57:30	468	124	9.9
05:58:00	581	119	8.8
05:58:45	282	113	8.5
05:59:45	438	116	9.7
06:00:45	614	130	10.1
06:02:00	1017	174	10.8

parameter to the change in the spectrum. If the contribution of variations in the selected parameter is very small, the accuracy of its determination is considered to be low as well.

CONCLUSION

In this work, we have carried out microwave diagnostics of flare plasma parameters by the direct fitting method, using data from the Siberian Radioheliograph and the proposed algorithm for restoring plasma and accelerated particle parameters. To test its efficiency, we applied the method to restoration of the parameters of model radio sources for cases when information about the frequency spectrum in different limited frequency ranges is available. We have demonstrated that the diagnostic results can be quite satisfactory even when the frequency range for observations with spatial resolution does not include spectral regions, where the source is optically thin.

We have selected the January 20, 2022 and July 16, 2023 flares for the diagnostics. For each flare, we have restored the following parameters, averaged over the maximum brightness region of the radio source: the electron density of background plasma n_0, the magnetic field strength B, the angle θ between the direction of the magnetic field and the line of sight θ, and the spectral index of energetic electrons δ_1. To analyze the dynamics of these parameters, the restoration was carried out at selected instants of time during the phases of rise, maximum, and decay in the intensity of individual emission peaks.

The values and dynamics of B, θ, and δ_1 for the two flares were shown to differ greatly. For the January 20, 2022, θ and δ_1 vary widely. The spectral index during the intensity rise phase decreases from 22 to 8.5 at the burst peak; and during the decay phase, it increases to 10.8. In the decay phase of the main peak, the angle between the line of sight and the direction of field lines decreases from 67° to 6°. For the January 20, 2022 flare, the magnetic field was as strong as ~1000 G. For the July 16, 2023 flare, the magnetic field strength is lower by an order of magnitude, and the energy spectrum index is 2–4 times lower; no strong changes in θ and δ_1 are recorded

For both flares, there are significant variations in the magnetic field in the region of maximum brightness of the radio source. During the rise phase of the main emission peaks, the magnetic field decreases, whereas during the decay phase, on the contrary, it increases. The rate of these variations is from a few to 11 G/s for the January 20, 2022 flare and is ~1 G/s for the July 16, 2023 flare. These values are comparable to the rate of field decrease obtained in [Fleishman et al., 2020, 2022] for the September 10, 2017 flare.

We believe that there are at least two possible reasons for such changes.

The first is that the detected changes are real field changes in some local fixed volume of the flare region. If we accept this hypothesis, far-reaching conclusions follow from it. According to the Faraday law, the high rate of field change at a given flare region should lead to generation of a very strong electric field several orders of magnitude higher than the Dreiser field and, accordingly, to a powerful acceleration of particles and heating of plasma, regardless of whether the field decreases or increases [Fleishman et al., 2020]. Fleishman et al. [2022] attribute the rapid decrease in the field they found to the process of dissipation of electric currents and their associated free magnetic energy of the field (its vortex component). The rapid increase in the field during the decay phase of flare emission peaks, we have detected in our work, does not fit this scheme. At the same time, it should be noted that in the literature [Solov'ev, Kirichek, 2023] the possibility is being discussed of restoring the magnetic field strength in the region of its rapid dissipation due to the transfer (with Alfvén velocity) of the field vortex component B_φ from the lower part of the twisted magnetic flux rope, where its pressure $B_\varphi^2/(8\pi)$ is noticeably higher than in the region of dissipation (the Parker effect, [Parker, 1979]).

The second possible reason is that there is some motion of the radio source brightness center from a region with a stronger magnetic field to a region with a weaker one and vice versa, which is unresolved by the radioheliograph.

Such a motion of the brightness center may be associated with two or more non-stationary emission sources within the beam pattern of the radioheliograph. If the brightness of these sources varies asynchronously with time, the resulting radio brightness redistribution between radio sources with a magnetic field of varying magnitude can be perceived as a time-varying magnetic field in a single source.

It is also possible that the motion of the brightness center may be related to the dynamics of the energetic electron distribution in a single flare loop with nonuniform magnetic field. This pattern of the maximum brightness motion along the flare loop is described in [Reznikova et al., 2009]; the authors analyze the dynamics of radio brightness distribution during a multicomponent burst observed at NoRH at 34 GHz in the August 24, 2002 flare. The authors have numerically calculated the dynamics of the spatial distribution of energetic electrons and their GS emission and have shown that the calculated motions of the maximum radio brightness between the footpoints of the magnetic loop, where the field is maximum, and the top of the loop, where the field is minimum, completely coincide with the observed ones. In our case, the dynamics of the angle between the magnetic field direction and the line of sight for the January 20, 2022 flare fits this scheme well. The motion of the maximum radio brightness to the footpoint of the flare loop may well be accompanied by a decrease in this angle if we observe the flare loop from above.

We tried to measure the motion of the radio source brightness center during the July 16, 2023 flare, for which an absolute coordinate reference was made to a distant sunspot. For this purpose, we applied the well-known method for positional interferometric measurements that can track the location of a radio source with an error significantly smaller than the antenna beam width. According to the method, in the case of a large signal-to-noise ratio (S/N), the error in positional measurements σ, based on finding the center of gravity in radio brightness distribution, turns out to be significantly smaller than the antenna beam half-width φ [Condon, 1997; Wu et al., 2024]:

$$\sigma \approx \frac{N}{S} \frac{\varphi}{2\sqrt{\ln 2}}. \tag{6}$$

For SRH data, S/N is usually >100; therefore, this method ensures the accuracy of positional measurements higher than 1".

The result of calculation of the brightness center motion for the July 16, 2023 flare is presented in Figure 15, where digits 1, 2, 3, ... 13 indicate the positions of the brightness center at a frequency of 11.8 GHz at the same time as in Figures 7 and 14. Compared to Figure 14, there are time points 8, 9, 10 here, for which radio diagnostics could not be performed. The red square in Figure 15 bounds the source region for which the frequency spectrum was calculated and the magnetic field was diagnosed. The fact that the brightness center moves during the flare is clearly seen. A monotonous shift occurs in the range of points 1–6 from the beginning of the rise phase of the first peak to the maximum of the second peak. Along the north—south direction, the maximum shift reaches 8"; and in the east–west direction, ~2". In this case, there is a significant decrease in the magnetic field strength (from 80 to 50 G, see Figure 14) only in the interval between points 4 and 6, corresponding to the rise phase of the second peak in the burst and to the brightness center shift by ~3.5".

During the third peak of the burst (points 11, 12, 13), the monotonous brightness center shift from north to south is also observed, but the magnetic field increases from
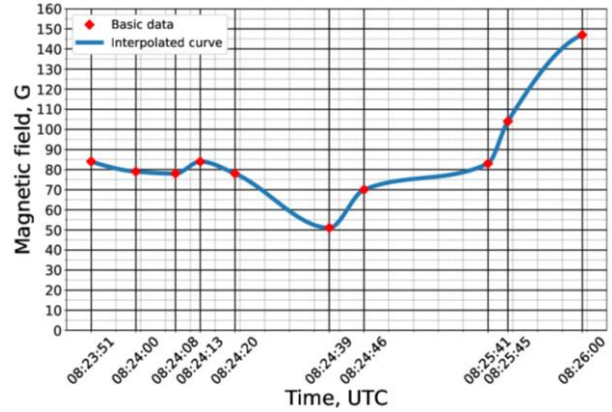

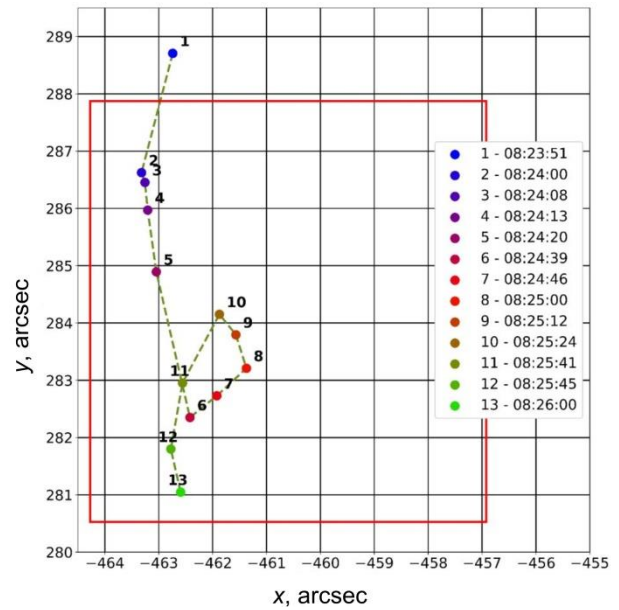*Figure 14.* Variation in the magnetic field strength during the July 16, 2023 flare

Figure 15. Trajectory of the radio source brightness center during the July 16, 2023 flare as observed by SRH at a frequency of 11.8 GHz

70 to 140 G. Note that points 6 (with the minimum field) and 11–13 (with the maximum field) are located close to each other (<1").

The analysis shows that at the moment we cannot unambiguously answer the question as to whether the detected magnetic field variations occur locally in a certain region or it is an effect of redistribution of radio brightness between regions of a complex radio source with different magnetic field strengths. Studies of new flares, preferably of noticeably large scales, are necessary in order to ensure their more reliable resolution by the radioheliograph. In December 2023, a new SRH antenna array in the 12–24 GHz range was put into operation. The use of new data on flares in this range will at least double the accuracy of positioning and hence will help in solving the above question about causes of magnetic field variations in radio sources of flares. Obviously, it is necessary to include data with high spatial resolution in the ultraviolet, hard and soft X-ray, and optical ranges in the analysis. It also makes sense to combine this analysis with restoration of the coronal magnetic field structure in a force-free approximation.

REFERENCES

Altyntsev A.T., Lesovoi S.V., Globa M.V., Gubin A.V., Kochanov A.A., Grechnev V.V., et al. Multiwave Siberian Radioheliograph. *Solar-Terr. Phys*. 2020, vol. 6, no. 2, pp. 30–40. DOI: 10.12737/stp-62202003.

Bogachev S.A., Somov B.V. Comparison of the Fermi and betatron acceleration efficiencies in collapsing magnetic traps. *Astrophys. J. Lett*. 2005, vol. 31, no. 8, pp. 537–545. DOI: 10.1134/1.2007030.

Christiansen U., Högbom I. *Radioteleskopy* [Radio telescopes]. Moscow, Mir Publ., 1988, p. 294. (In Russian).

Condon J.J. Errors in Elliptical Gaussian Fits. *Publications of the Astronomical Society of the Pacific*. 1997, vol. 109, pp. 166–172. DOI: 10.1086/133871.

Dulk G. Radio emission from the Sun and stars. *Ann. Rev. Astron. Astrophys*. 1985, vol. 23, pp. 169–224. DOI: 10.1146/annurev.aa.23.090185.001125.

Fleishman G.D., Melnikov V.F. Gyrosynchrotron emission from anisotropic electron distributions. *Astrophys. J*. 2003, vol. 587, no. 2, pp. 823–835. DOI: 10.1086/368252.

Fleishman G.D., Kuznetsov A.A. Fast gyrosynchrotron codes. *Astrophys. J*. 2010, vol. 721, no. 2, pp. 1127–1141. DOI: 10.1088/0004-637X/721/2/1127.

Fleishman G.D., Nita G.M., Gary D.E. Dynamic magnetography of solar flaring loops. *Astrophys. J. Lett*. 2009, vol. 698, no. 2, pp. 183–187. DOI: 10.1088/0004-637X/698/2/L183.

Fleishman G.D., Gary D.E., Chen B., Kuroda N., Yu S., Nita G.M. Decay of the coronal magnetic field can release sufficient energy to power a solar flare. *Science*. 2020, vol. 367, no. 6475, pp. 278–280. DOI: 10.1126/science.aax6874.

Fleishman G.D., Nita G.M., Chen B., Yu S., Gary D.E. Solar flare accelerates nearly all electrons in a large coronal volume. *Nature*. 2022, vol. 606, pp. 674–677. DOI: 10.1038/s41586-022-04728-8.

Gary D.E., Fleishman G.D., Nita G.M. Magnetography of solar flaring loops with microwave imaging spectropolarimetry. *Solar Phys*. 2013, vol. 288, no. 2, pp. 549–565. DOI: 10.1007/ s11207-013-0299-3.

Gary D.E., Chen B., Dennis B.R., Fleishman G.D., Hurford G.J., Krucker S., et al. Microwave and hard X-ray observations of the 2017 September 10 solar limb flare. *Astrophys. J*. 2018, vol. 863, no. 1, 9 p. DOI: 10.3847/1538-4357/aad0ef.

Kuznetsov S.A., Melnikov V.F. Modeling the effect of dense plasma on the dynamics of the microwave spectrum of solar flaring loops. *Geomagnetism and Aeronomy*. 2012, vol. 52, no. 7, pp. 883–891. DOI: 10.1134/S0016793212070092.

Morgachev A.S., Kuznetsov S.A., Melnikov V.F. Radio diagnostics of the solar flaring loop parameters by direct fitting method. *Geomagnetism and Aeronomy*. 2014, vol. 54, no. 7, pp. 933–942. DOI: 10.1134/S0016793214070081.

Parker E.N. *Cosmical Magnetic Fields*. Part 1. Clarendon Press, Oxford, 1979.

Razin V.A. To the theory of radio emission spectra caused by discrete sources at frequencies lower than 30 MHz. *Izvestiya vysshih uchebnyh zavedenij. Radiofizika* [News of higher educational institutions. Radiophysics]. 1960, vol. 3, no. 4, pp. 584–594. (In Russian).

Reznikova V.E., Melnikov V.F., Shibasaki K., Gorbikov S.P., Pyatakov N.P., Myagkova I.N., Ji H. 2002 August 24 limb flare loop: dynamics of microwave brightness distribution. *Astrophys. J*. 2009, vol. 697, pp. 735–746. DOI: 10.1088/0004-637X/697/1/735.

Solov'ev A.A., Kirichek E.A. Properties of the flare energy release in force-free magnetic flux ropes. *Astron. Lett*. 2023, vol. 49, no. 5, pp. 257–269. DOI: 10.1134/S1063773723050055.

Somov B.V., Kosugi T. Collisionless reconnection and high-energy particle acceleration in solar flares. *Astrophys. J*. 1997, vol. 485, no. 2, pp. 859−868. DOI: 10.1086/304449.

Wu Zh., Kuznetsov A., Anfinogentov S., Melnikov V., Sych R., et al. A multipeak solar flare with a high turnover frequency of the gyrosynchrotron spectra from the loop-top source. *Astrophys. J*. 2024, vol. 968, no. 1, 11 p. DOI: 10.3847/1538-4357/ad46ff.

Yan Y., Chen Z., Wang W., Liu F., Geng L., Chen L., et al. Mingantu spectral radioheliograph for solar and space weather studies. *Frontiers in Astronomy and Space Sciences*. 2021, vol. 8:584043. DOI: 10.3389/fspas.2021.584043.

Zirin H., Baumert B.M., Hurford G.J. The microwave brightness temperature spectrum of the quiet Sun. *Astrophys. J*. 1991, vol. 370, pp. 779–783. DOI: 10.1086/169861.